Available online at www.sciencedirect.com
SCIENCE DIRECT
Free Radical Biology & Medicine 40 (2006) 407 – 419
www.elsevier.com/locate/freeradbiomed

Original Contribution

Cycloimide bacteriochlorin *p* derivatives: Photodynamic properties and cellular and tissue distribution

George V. Sharonov [a], Tatyana A. Karmakova [b], Roel Kassies [c], Anna D. Pljutinskaya [b], Michael A. Grin [d], Matthieu Refregiers [e], Raisa I. Yakubovskaya [b], Andrey F. Mironov [d], Jean-Claude Maurizot [e], Paul Vigny [e], Cees Otto [c], Alexei V. Feofanov [a,*]

[a] *Shemyakin-Ovchinnikov Institute of Bioorganic Chemistry, Russian Academy of Sciences, ul. Miklukho-Maklaya 16/10, 117997 Moscow, Russia*
[b] *Hertsen Moscow Oncological Institute, 2nd Botkinskiy pr., 3, 125284 Moscow, Russia*
[c] *University of Twente, Faculty of Science and Technology, Biophysical Techniques, Biomedical Technology Institute, P.O. Box 217, 7500 AE Enschede, The Netherlands*
[d] *Lomonosov State Academy of Fine Chemical Technology, Vernadskogo pr., 86, 119571 Moscow, Russia*
[e] *Centre de Biophysique Moleculaire, CNRS UPR 4301, affiliated to the University of Orleans and to Inserm, rue Charles-Sadron, 45071 Orleans, France*

Received 19 April 2005; revised 16 August 2005; accepted 19 August 2005
Available online 17 October 2005

Abstract

Reactive oxygen species generated by photosensitizers are efficacious remedy for tumor eradication. Eleven cycloimide derivatives of bacteriochlorin *p* (CIBCs) with different N-substituents at the fused imide ring and various substituents replacing the 3-acetyl group were evaluated as photosensitizers with special emphasis on structure–activity relationships. The studied CIBCs absorb light within a tissue transparency window (780–830 nm) and possess high photostability at prolonged light irradiation. The most active derivatives are 300-fold more phototoxic toward HeLa and A549 cells than the clinically used photosensitizer Photogem due to the substituents that improve intracellular accumulation (distribution ratio of 8–13) and provide efficient photoinduced singlet oxygen generation (quantum yields of 0.54–0.57). The substituents predefine selective CIBC targeting to lipid droplets, Golgi apparatus, and lysosomes or provide mixed lipid droplets and Golgi apparatus localization in cancer cells. Lipid droplets and Golgi apparatus are critically sensitive to photoinduced damage. The average lethal dose of CIBC-generated singlet oxygen per volume unit of cell was estimated to be 0.22 mM. Confocal fluorescence analysis of tissue sections of tumor-bearing mice revealed the features of tissue distribution of selected CIBCs and, in particular, their ability to accumulate in tumor nodules and surrounding connective tissues. Considering the short-range action of singlet oxygen, these properties of CIBCs are prerequisite to efficient antitumor photodynamic therapy.

Keywords: Near-IR photosensitizer; Cycloimide bacteriochlorin *p*; Singlet oxygen; Photodynamic; Confocal; Free radicals

Introduction

Recent achievements in photodynamic therapy (PDT) demonstrate that reactive oxygen species (ROS) are an efficacious remedy for tumor eradication [1,2]. Local activation of ROS production with red light and the short-range damaging action of ROS are advantageous in providing selective treatment of localized tumors with PDT and in avoiding general toxicity, which is a concurrent feature of chemotherapy and X-ray treatment. PDT efficiency is tightly related to the properties of the photosensitizer, an organic dye that harvests light and produces ROS in energy transfer or redox reactions

Abbreviations: AO, acridine orange; BODIPY ceramide, *N*-((4-(4,4-difluoro-5-(2-thienyl)-4-bora-3a, 4a-diaza-s-indacene-3-yl) phenoxy)acetyl)-sphingosine; CIBC(s), cycloimide derivative(s) of bacteriochlorin *p*; CIC(s), cycloimide derivative(s) of chlorin p6; CrEL, polyoxyethylene derivative of hydrogenated castor oil, Cremophor EL; CSI, confocal spectral imaging; DR, distribution ratio, a ratio of average cytoplasmic concentration to the extracellular concentration of a photosensitizer; FCS, fetal calf serum; LSCM, laser scanning confocal microscopy; MTT, 3-(4,5-dimethylthiazole-2-yl)-2,5-biphenyl tetrazolium bromide; NIR, near infrared; PDT, photodynamic therapy; Φ_Δ, singlet oxygen quantum yield; RNO, 4-nitroso-*N,N*,-dimethylaniline; Rh123, rhodamine 123; ROS, reactive oxygen species.

* Corresponding author. Fax: +7 095 3361766.
E-mail address: alexei@nmr.ru (A.V. Feofanov).

0891-5849/$ - see front matter © 2005 Elsevier Inc. All rights reserved.
doi:10.1016/j.freeradbiomed.2005.08.028

but is not toxic to cells itself. Advanced photosensitizers are required for further progress of PDT. They should have improved accumulation in malignant tissue and penetration in tumor cells and possess high yield production of ROS and intensive absorption in the near-infrared (NIR) region (750–850 nm), where tissues have increased transparency for the exciting light.

Derivatives of bacteriochlorophyll *a* are intrinsically suitable for PDT. They absorb at 760–780 nm and are capable of photoinduced ROS production, but their photostability is rather low. Because of their attractive photodynamic properties, considerable efforts are spent to develop new bacteriochlorophyll-based photosensitizers [3–12]. Recently synthesis of cycloimide derivatives of bacteriochlorin *p* (CIBCs) was realized, providing a bathochromic shift of bacteriochlorin *p* absorption to the 780–830 nm region and improved photostability of the molecule [8–14]. Moreover, the fused imide ring, 3-acetyl, and 17-propionic acid groups of CIBCS can be further subjected to site-directed modification in order to achieve high tumor affinity for the derivatives. This is an evident advantage of CIBCs over other ROS-generating NIR dyes like naphtalocyanines or, for example, 5,10,15,20-tetra(3-hydroxyphelyl)bacterichlorin. The noted compounds are symmetric molecules, thereby substitutions occur at several sites simultaneously, and the exact positions of substituents are poorly predictable.

A series of alkyl ether derivatives of *N*-hexyl cycloimide bacteriochlorin *p* (**12**–**15**, Fig. 1) was synthesized recently [11,12]. In vitro and in vivo studies revealed high photodynamic activity of these compounds and pronounced dependence of their relative activity on the length of 3-deacetyl-3-(1-alkyloxy)ethyl substituent [11]. Differences in PDT efficacy were found for the *S* and *R* isomers of the most active 3-deacetyl-3-(1-heptyloxy)ethyl derivative [12]. It was reported that one CIBC was selected for human preclinical and clinical trials [12].

Synthesis of *N*-hydroxycycloimide and *N*-aminocycloimide bacteriochlorin *p* derivatives was developed [8–10,13,14]. Many of these CIBCs are phototoxic to tumor cells as demonstrated in our preliminary studies [8,15]. Here we present a detailed report on the PDT relevant properties of compounds **1**–**11** (Fig. 1) including intracellular accumulation and localization. Moreover, accumulation and distribution of **2**, **5**, **7**, and **8** in murine tumor tissue was measured and found to be promising for efficient PDT.

CIBCs as other photosensitizers fluoresce and thereby are detectable in tissues and cells with fluorescence microscopy. This would facilitate rational drug design, because the simple answer “yes” or “no” obtained with activity assays can be complemented with the data of fluorescence microscopy explaining “why” and “how.” ROS have very short lifetime and short diffusion distance from the site of their production. Therefore, photosensitizer localization points out the cellular and tissue structures subjected to ROS impact. Local concentrations of photosensitizer predefine the intensity of ROS production, which should be high enough to overcome antioxidative and reparative defense systems of target cells.

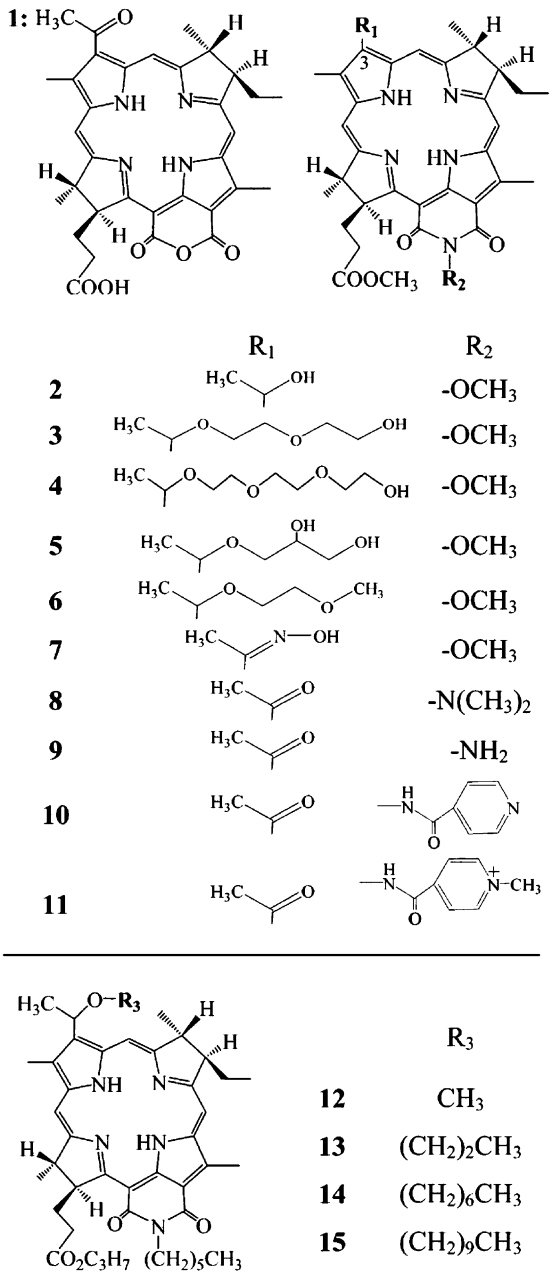

Fig. 1. Structures of bacteriopurpurin **1** and cycloimide derivatives of bacteriochlorin *p* **2**– **15**.

Both localization and concentration of photosensitizers can be revealed and compared in living cells and tissue sections using confocal spectral imaging (CSI) techniques [16–20]. At the same time commercial laser scanning confocal microscopes (LSCM) have low sensitivity for the NIR spectral region. Accordingly, highly sensitive NIR-LSCM was created and employed here to support microscopy study of CIBCs, when sensitivity of an installation for the CSI measurements and commercial LSCM were insufficient.

We demonstrate that varying the structure of the substituents high intracellular concentration, controlled localization, and, finally, improved activity of CIBC can be achieved. Our findings highlight the importance of CIBC structure optimiza-

tion as a way of targeting the photosensitizer to specific cellular organelles and improving its cellular accumulation and tumor selectivity.

Material and methods

Chemicals

Compounds **1** [10], **2** [13], **7**[9], **8**, **9** [8], **10,** and **11** [14] were synthesized as described earlier.

3α-Hydroxyethyl group of **2** was activated with anhydride of trifluoroacetic acid (Scheme 1). The reaction was carried out in dichloromethane for 20 min (20°C) and monitored with spectrophotometry and chromatography. Product **2a** absorbs at 803 nm and has higher chromatographic mobility than **2**. Compounds **3**–**6** were obtained by incubating **2a** with monomethyl ether of ethylene glycol (**6**), glycerol (**5**), diethylene glycol (**3**), and triethylene glycol (**4**). Reaction time depended on the substituent structure and varied from 10 min for **6** to 12 h for **5**. The products absorb at 792 nm and have less chromatographic mobility than **2a**. The structure of **3**–**6** was confirmed with mass spectra measured with the MALDI technique.

3. MS, *m/z* (%): 715.2 ($[M]^+$, 50), 684.2 ($[M]^+-OCH_3$, 50).
4. MS, *m/z* (%): 759.5 ($[M]^+$, 100).
5. MS, *m/z* (%): 701.4 ($[M]^+$, 100).
6. MS, *m/z* (%): 685.4 ($[M]^+$, 100).

Stock solutions of CIBCs were prepared by chafing the CIBC powders in a small quantity of 100% Cremophor EL (polyoxyethylene derivative of hydrogenated castor oil, CrEL) and watering them down to 10% CrEL. CIBC concentrations in aqueous solutions were measured in the presence of 5% CrEL with spectrophotometry using extinction coefficients listed in Table 1.

Acridine orange (AO) and rhodamine 123 (Rh123) were purchased from ICN (Costa Mesa, CA). L-Histidine, 4-nitroso-*N,N*-dimethylaniline (RNO) and CrEL were supplied by Sigma (St. Louis, MO). *N*-((4-(4,4-Difluoro-5-(2-thienyl)-4-bora-3a,4a-diaza-s-indacene-3-yl)phenoxy) acetyl) sphingosine (BODIPY ceramide) was purchased from Molecular Probes Inc. (Eugene, OR). Nile Red and Rose Bengal were purchased from DiaM (Moscow, Russsia). The other chemicals used in this work were of analytical reagent grade.

Detection of ROS

Detection of light-induced ROS generation by CIBC in solution was performed using the approved procedures as described earlier [16–18,21]. The reaction of RNO bleaching with hydroxyl (•OH) radicals [22] allowed us to check if CIBCs produce •OH under light irradiation (Nd^{3+}–YAG laser, 532 nm, 1 mW). Singlet oxygen generation was assessed with the same assay in the presence of histidine [21]. Reacting with histidine, singlet oxygen produces *trans*-annular peroxide intermediate, which, in its turn, oxidizes RNO.

Air-equilibrated solutions of CIBC in 0.1–0.3% CrEL (50 mM Tris–HCl, pH 7.2) contained 30 μM RNO and (if necessary) 0.1 mM histidine. Bleaching of RNO was monitored with spectrophotometry at 440 nm and corrected for contribution of CIBC absorption at this wavelength. Singlet oxygen quantum yields (Φ_Δ) were calculated comparing the rates of RNO bleaching by CIBC in 1% CrEL and Rose Bengal in water (Φ_Δ = 0.75 [23]) under the same experimental conditions. Concentrations of CIBC and Rose Bengal were adjusted to provide an equal absorption (0.06 optical unit/cm) at 532 nm.

Cells and their treatment

Human cervix epitheloid carcinoma HeLa cells and human lung adenocarcinoma A549 cells were grown (37°C, 5% CO_2) in a complete medium: Dulbecco's minimum essential medium without phenol red supplemented with 10% fetal calf serum (FCS), 2 mM L-glutamine (HeLa cells); Eagle's minimum essential medium with phenol red, 10% FCS, 2 mM L-glutamine (A549 cells).

For the survival assays cells were seeded into 96-well plates. Twenty-four hours later, CIBCs were added gradually into the wells to achieve concentrations ranging from 0.007 to 4 μM with a twofold increment. The cytotoxicity was determined after a 26-h incubation of cells with CIBC in the dark. Note that incubation of cells with up to 0.01% CrEL for 26 h did not induce a noticeable cytotoxicity [16,17]. The phototoxicity was determined on cells incubated with CIBC in a complete medium for 3 h, placed in the dye-free medium, and irradiated.

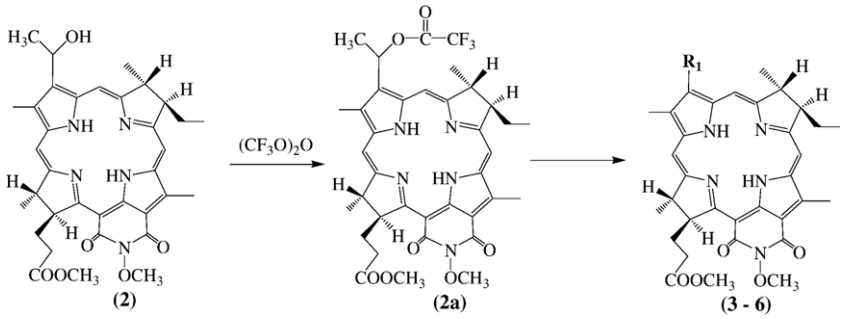

Scheme 1.

Table 1
Solubility in CrEL, phototoxicity toward HeLa and A549 cells, and photochemical and cellular characteristics of CIBCs

Compound	**1**	**2**	**3**	**4**	**5**	**6**	**7**	**8**	**9**	**10**	**11**
Solubility in 10% CrEL (mM)	0.5	2.1	1.4	1.2	1.6	1.2	0.6	0.4	0.6	1.1	0.8
λ_Q (nm)	812	778	782	780	782	783	793	821	832	827	828
λ_{em} (nm)	821	794	797	797	797	799	809	831	840	840	842
$\varepsilon(\lambda_Q)$[a] $\times 10^{-3}$ ($M^{-1} \times cm^{-1}$)	12	31	29	32	24	28	27	50	15	21	30
Φ_Δ[b]	0.27 ± 0.03	0.54 ± 0.04	0.55 ± 0.04	0.54 ± 0.02	0.55 ± 0.02	0.57 ± 0.03	0.51 ± 0.01	0.39 ± 0.02	0.24 ± 0.03	0.19 ± 0.04	0.07 ± 0.02
Φ_{PB}[c] $\times 10^6$ ±10%	N/D	0.7	1	1	1	0.7	0.9	0.6	0.7	0.5	N/D
IC_{90}(A549 cells)[d] (nM)	1000 ± 100	70 ± 15	60 ± 10	60 ± 5	60 ± 10	80 ± 10	45 ± 5	170 ± 20	490 ± 90	220 ± 40	>1000
IC_{90}(HeLa cells) (nM)	1100 ± 130	60 ± 10	60 ± 10	60 ± 5	60 ± 5	60 ± 5	50 ± 5	90 ± 10	440 ± 50	500 ± 90	>1000
DR (HeLa cells)[e] ±5%	0.37	4.7	10.4	8.5	7.9	13.1	2.3	3.8	3.4	1.6	0.6
$LD_{90}(^1O_2)$[f] (mM)	0.06	0.18	0.34	0.37	0.22	0.41	0.06	0.18	0.22	0.13	
Localization (LD/Golgi)	**/***	***/**	***/**	***/**	*/****	***/**	***/**	****/*	****/*	*/****	L[g]

[a] Molar extinction coefficient in 1% CrEL emulsion at the Q-band maximum, λ_Q.
[b] Singlet oxygen quantum yield in 0.1–0.3% CrEL emulsion. Mean ± SE.
[c] Photobleaching quantum yield in 0.1–0.3% CrEL emulsion.
[d] Extracellular concentration of photosensitizer that induces 90% inhibition of cell growth under the incubation and irradiation conditions described under Materials and methods.
[e] Distribution ratio, a ratio of the average cytoplasmic concentration to the extracellular concentration of a photosensitizer measured after 3 h of incubation with 1 μM of the photosensitizer in a complete medium.
[f] Amount of singlet oxygen per volume unit of cell generated during irradiation that provides 90% cytotoxicity for HeLa cells.
[g] Lysosomal localization is supposed.

The irradiation of the cells (11 ± 1 mW/cm^2, 15 min) was carried out with a 500 W halogen lamp through a 5-cm water filter and a bandpass filter (transmission 700–1000 nm). The cell viability was estimated 24 h after irradiation with the 3-(4,5-dimethylthiazole-2-yl)-2,5-biphenyl tetrazolium bromide (MTT) assay according to a procedure described elsewhere [24]. Phototoxic responses were fitted with sigmoid dose–response curves, and concentrations that induced 90% inhibition of cells growth (IC_{90}) were determined. Earlier, we have demonstrated that this assay performed 24 h after irradiation of cells loaded with cycloimide derivatives of chlorin p6 (CICs) is a true viability assay if the IC_{90} value is considered as an indicator of drug phototoxicity [16].

MTT assay is based on the reduction of MTT to colored formazan by enzymes of living cells. Since there is a definite probability to overestimate the cell killing ability of CIBCs due to temporal suppression of a MTT reducing enzymatic activity, we have again verified that the assay results are not time dependent. The MTT assay was performed 24 and 48 h after the irradiation of control HeLa cells and the HeLa cells were loaded with compounds **2** and **5**. When cells were incubated with a low concentration of **2** (**5**) and irradiated, the MTT assay did provided a time-dependent value of viable cells: 39% (40%) after 24 h and 58% (83%) after 48 h. However, no time-dependent increase in an apparent cell viability was observed with the MTT assay when cells were loaded with **2** (**5**) at the concentration providing 10% or less of viable cells. Additionally, we have measured the photoinduced cytotoxicity of **2** and **5** using a fluorescence microscopy approach. Cells were stained with Hoechst 33342 (it stains nuclei of all cells) and propidium iodide (it stains nuclei of dead cells), and the IC_{90} values determined by the direct count of dead cells coincided well with the data of the MTT assay.

For microscopic measurements cells were seeded in 24-well plates (onto cover glasses) a day prior to an experiment. Concentration dependence of uptake was measured on HeLa cells incubated with 0.1–7 μM CIBC in the complete medium for 3 h at 37°C. For efflux experiments cells were incubated with CIBC (2 μM for 3 h) in the complete medium, rinsed twice with a fresh medium, and grown for 2 h in a dye-free complete medium.

For staining the Golgi apparatus, the thoroughly washed A549 cells were incubated with the complex of BODIPY ceramide and bovine serum albumin (5 μM for 15 min) in Hanks' balanced salt solution at 37°C, rinsed, and incubated with CIBC (2 μM) for 1 h in the complete medium at 37°C. To identify lipid droplets, A549 cells were incubated jointly with Nile Red (0.5 μM added from 50 μM stock solution in 0.1% CrEL) and CIBC (2 μM) for 2 h at 37°C. To identify mitochondria and lysosomes, A549 cells were incubated with 0.5 μM Rh123 or 1 μM AO (15 min, 37°C) after incubation with CIBC (2–4 μM for 2 h, 37°C).

To probe the state of lysosomes and mitochondria after irradiation, the cells were loaded with selected CIBCs (compounds **2**, **5**, **6,** and **8** were used in this study), irradiated, and 1 h later stained with Rh123 (0.5 μM) or AO (1 μM). The functioning of lipid transport was checked with the following procedure: 1 h after irradiation the cells were washed carefully and incubated with BODIPY ceramide (5 μM, 15 min, 37°C) in Hanks' balanced salt solution, rinsed, and placed in a complete medium for 30 min. The results of these experiments were

compared at ca. 50 and 100% levels of phototoxicity achieved by varying CIBC concentrations.

Finally, cells attached to the cover glass were placed on a microscope slide, humidified with Hank's balanced salt solution (60 μl), covered with a coverslip, and placed on a microscope stage.

Experiments with animals

Female mice C57Bl/6j × DBA/2 were purchased from the rodent breeding colony (Stolbovaya, Russia) and maintained under pathogen-free conditions. P388 lymphoid leukemia cells were passaged serially in mice in ascitic form. Ten-to 12-week-old mice (body weight of 21 ± 1 g) were subcutaneously inoculated with tumor cell suspension (0.1 ml containing (1.0 ± 0.2) × 10^6 cells) in the right hind paw (lymphoma-like model). Mice were injected with CIBC (0.5 mg/ml in 10% CrEL; dose of 10 mg per kg of body weight) intraperitoneally at 8 days of tumor growth. Three hours after injection tissue sections of 10 μm thickness were prepared with cryotome, studied with NIR-LSCM, and, finally, fixed and stained with hematoxylin and eosin.

Fluorescence microscopy measurements and analysis of data

Measurements of CIBC intracellular fluorescence spectra and simulation of their intracellular environment in solution were performed with a V-45 installation (DILOR SA, Lille, France) for confocal spectral imaging analysis. The CSI technique was used also to identify the sites of CIBC intracellular accumulation. The measurements were carried out with a 100× oil-immersion objective (Nikon, Japan) at ca. 0.6 μm lateral and ca. 3 μm axial resolution. The CSI technique was based on measurement of the spectrum at each point of a specimen [25,26]. The spectral resolution was 1 nm. The 40 × 30 or 60 × 40 voxel spectral images were recorded depending on the task using a He,Ne laser (543.5 nm, 17 μW). The accumulation and treatment of the spectral images were performed as described previously [16–18,25,26].

To identify the sites of CIBC intracellular accumulation LSCM 510META (Carl Zeiss AG, Germany) was also used. The sensitivity of LSCM 510META was sufficient to detect CIBC fluorescence in the A549 cells only if CIBC fluoresced at 800 nm or at a shorter wavelength and its average intracellular concentration was higher than 8 μM. The 1024 × 1024 voxel confocal images were recorded with a 63 × C-Apochromat water immersion objective (NA = 1.2, Carl Zeiss AG) at ca. 0.4 μm lateral and ca. 2 μm axial resolution. The following optical path was used to discriminate the fluorescence of selective organelle probes and CIBC: fluorescence was excited with a HeNe laser (543.5 nm, ca. 100 μW on the sample), and a backscattered signal passed through the 488/543.5 Hilbert transform filter and split with the 650-nm dichroic mirror. The long-wavelength fluorescence, which passed through the mirror, was dispersed into a spectrum with a grating and focused at the META detector (an array of 32 microphotomultipliers). The signal recorded by the META detector in the 788–799 nm spectral range was considered as a CIBC fluorescence. The signal recorded by the META detector in the 650–670 nm spectral range was considered as a fluorescence of aggregated AO in lysosomes or as a red component of Nile Red fluorescence. The short-wavelength fluorescence, which was reflected by the 650-nm dichroic mirror, was additionally filtered with the 545-nm dichroic mirror and the 560-to 615-nm band-path filter and directed to a photomultiplier. This detection channel was used to record green-yellow fluorescence of a probe, i.e., Rh123, BODIPY ceramide, monomeric AO, and green component of Nile Red fluorescence. The same configuration of LSCM 510META was used to probe the state of organelles after irradiation of cells loaded with CIBC. The control measurements of the cells stained with CIBC alone or with each selective organelle probe alone confirmed that the CIBC signal did not contribute to the probe detection channel, and the probe signal did not contribute to the CIBC detection channel.

Low sensitivity of the V-45 installation and LSCM 510META in the 750–850 nm region restricted applicability of these devices to the study of CIBCS in cells. Reliable detection of the weak intracellular signals of CIBC was achieved with the newly developed NIR-LSCM. Design of NIR-LSCM is briefly the following: a laser beam of the 800-nm diode laser (10 μW on the sample) is focused onto the sample by an objective; fluorescence signal collected with the same objective passes through the 850-nm dichroic mirror and confocal pinhole (25 μm in diameter) to an avalanche photodiode detector; up to 40 × 40 μm specimen area is scanned with a piezoelectric stage. As low as 20–40 CIBC molecules per voxel (ca 0.5 μm^3) were reliably detected in solution, within living cells or tissue structures with NIR-LSCM. NIR-LSCM was used to measure the detailed intracellular and tissue distributions of CIBC and to perform the quantitative analysis of CIBC accumulation in cells and tissue structures. Note that construction of NIR-LSCM is not suitable for double-staining experiments.

The 128 × 128 or 256 × 256 voxel confocal fluorescence images were recorded from living cells with a 100× oil-immersion objective (NA = 1.25) at ca. 0.4 μm lateral and ca. 2 μm axial resolution. Intracellular CIBC concentrations were calculated on the basis of CSI and NIR-LSCM measurements. The CSI study helped to reveal the composition of a model solution (1% CrEL, 50 mM Tris–HCl, pH 7.2), which mimicked the CIBC intracellular environment as judged by a coincidence of CIBC fluorescence spectra in cells and in the model solution. The intracellular CIBC concentrations were estimated by comparing fluorescence intensities from the equal voxels of a cell and the model solution with a known concentration of CIBC. This approach is based on the perfect confocal properties of NIR-LSCM and lack of background signal and justified by the linear dependence of fluorescence intensity on the CIBC concentration in the model solution. Data on intracellular CIBC concentrations were averaged over three independent experiments, and each experiment included analysis of 10–15 cells.

Assuming that efflux kinetics of CIBC can be described with simple exponential dependence as for the CICs [17,18], time for

50% dye release (T_{ef}) was estimated in minutes on the basis of the average cytoplasmic concentrations of the dye at the moment, when the dye was removed from the extracellular medium ($C_{cyt}(0)$), and 2 h after that ($C_{cyt}(2)$).

$$T_{ef} = 120 \cdot \ln 2 / \ln\left(C_{cyt}(0)/C_{cyt}(2)\right). \quad (1)$$

This estimation was performed using the data of two independent experiments.

The 128 × 128 voxel confocal fluorescence images were acquired from tissue sections with a 50 × dry objective (NA = 0.9) at ca. 0.4 μm lateral and ca. 3 μm axial resolution. Estimation of CIBC concentration in tissue sections was done in a similar way as for cells. To account for the changes in fluorescence intensity due to reduced water content in tissue after deep freezing we have compared the intensity of CIBC fluorescence in the living and dried cells. Fluorescence intensity was reduced 1.3-fold in dried cells as compared to living cells. Accordingly, fluorescence intensities measured from tissue sections were corrected for this factor.

The software processing of confocal fluorescence images was performed in order to average the concentration of CIBCs in various tissue structures identified histochemically.

Results

CIBCs and **1** are not soluble in water but can be solubilized with water emulsions of CrEL. CrEL protects CIBCs and **1** against aggregation even after extended dilution in water, if an optimal dye/CrEL ratio is used. From our experience, preservation of the monomeric form is important for efficient intracellular penetration of hydrophobic porphyrin derivatives [16–18]. Solubilities of **1**–**11** in 10% CrEL are listed in Table 1. An increase in the dye/CrEL ratio above the optimal value results in aggregation and precipitation of CIBC excess. A monomeric form of CIBC becomes more stable, if the CrEL concentration increases, but a decrease in the dye/CrEL ratio is undesirable, since a high concentration of CrEL is toxic for cells [16–18].

Depending on the substituent groups the long-wavelength absorption of CIBCs varies from 778 to 832 nm (Table 1). Substituents that interact with a π-electronic system of the macrocycle (**7**–**11**) provide the largest bathochromic shift of the long-wavelength absorption. Molar extinction coefficients of CIBCs are higher than that of bacteriopurpurin *a* carboxylic acid (**1**), a substrate for CIBC synthesis.

Compounds **1**–**8, 10,** and **11** are stable on storage in water–CrEL solutions for a month, whereas the structure of **9** is subjected to a modification in the solution for 24 h. This modification manifests itself as a 5-nm blue shift of the long-wavelength Q band and broadening of all the absorption bands.

In vitro activity

Compounds **1**–**10** provide photoinduced damage of the HeLa and A549 cells, but photosensitizing efficacy (estimated with IC_{90} values) depends considerably on the dye structure (Table 1). The sensitivities of HeLa and A549 cells to photodynamic effect produced with **1**–**10** are similar (Table 1). Cell growth is not affected with the studied compounds in the dark or with the light irradiation without photosensitizers.

The IC_{90} values were less than 0.5 μM for compounds **2**–**10**. The CrEL concentration was less than 0.008% in these experiments, and the cytotoxicity of CrEL did not contribute to the observed effect. The IC_{90} value of **1** (Table 1) was corrected for a small contribution of CrEL cytotoxicity. Compound **11** is not phototoxic to the cells, since concentration–response curves of the irradiated cells preincubated with **11** and CrEL alone were very similar.

Photoinduced cell-killing efficacy of the most active 13,15-*N*-methyl ester derivatives (**2**–**7**) is ca. 300 times higher than that of the clinically used photosensitizer, Photogem (Russian analog of Photophrin), and ca. 20 times higher that that of **1**. This comparison was done on the basis of dye concentrations killing 90% of cells at a standard light dose. The structure of the R_1 group in **2**–**7**does not affect photoinduced cytotoxicity. A combination of 3-acetyl group and R_2 substituents conjugated through the N–N bond results in the reduced activity of **8** and, especially, **9, 10,** and **11** (Table 1).

The studies discussed below were undertaken to clarify key mechanisms of the CIBC photosensitizing action and to understand the reasons of the substantial differences in CIBC activities. The primary photodynamic action is initiated with ROS, and they have a short lifetime in a biological environment. Therefore, we have focused our attention on the ability of CIBC to generate ROS and on the photosensitizer distribution in cells and tissues, as a pointer of both ROS generation sites and localization of ROS targets.

Photophysical properties of CIBC

CIBCs do not produce hydroxyl radicals when CIBC solutions are irradiated with light. They possess a light-induced generation of singlet oxygen in water–CrEL solutions, in 1% Triton X-100 solutions, and in lecithin liposomes. Characteristic intensive fluorescence spectra of CIBCs indicate that CIBCs are in a monomeric form in these lipid systems. If CIBCS are aggregated when, for example, watered down from dimethyl sulfoxide or ethanol stock solution, they do not fluoresce and do not produce singlet oxygen. According to the Φ_Δ values measured for CIBCs in 1% CrEL (Table 1) a singlet oxygen generation ability decreases in the order **2** ≈ **3** ≈ **4** ≈ **5** ≈ **6** ≈ **7** > **8** > **1** > **9** > **10** > **11**. The differences in Φ_Δ are responsible at least partially for the differences in CIBC phototoxicities in vitro (Table 1).

NIR photosensitizers are approaching the limit where the energy of their lowest triplet state becomes smaller than the energy required for singlet oxygen production (7900 cm^{-1}) and Φ_Δ decreases considerably. This is probably the case for **8**–**10** with the longest wavelength absorption but not for **2**–**7** (Table 1), since Φ_Δ for **2**–**7** are of the same value as Φ_Δ for CICs with λ_Q = 710 nm [16–18]. In addition, the structure of chromophore and substituents affects Φ_Δ. For example, Φ_Δ of **8** (λ_Q = 821 nm) is higher than Φ_Δ of **1** (λ_Q = 812 nm) and Φ_Δ

of **9** (λ_Q = 832 nm) is higher than Φ_Δ of **11** (λ_Q = 828 nm) and Φ_Δ of **10** (λ_Q = 827 nm).

Intracellular accumulation and localization

The CSI measurements show that CIBCs penetrate inside cells and accumulate there in a monomeric photoactive form. Intracellular fluorescence spectra of **2**–**8** are very similar to those in CrEL emulsion, Triton X-100 micelles, and lecithin liposomes (Table 1), thus indicating that CIBCs are most probably situated in a lipid environment in cells. This fact is consistent with CIBC hydrophobicity.

Detailed study with NIR-LSCM revealed prominent structure-dependent differences in CIBC intracellular distribution. At least two distinct localization patterns were recognized: accumulation in granules (ca. 0.8 μm diameter) and homogeneous staining of cytoplasm with enhanced accumulation in the perinuclear region. The observed distribution is always a superposition of both patterns but their relative contribution depends on the structure of the R_1 and R_2 substituent groups (Fig. 2). Granular distribution dominates for **8**, **9,** and **11**. It is significant for **2**–**4**, **6**, and **7** and relatively weak for **1**, **5,** and **10**. Except for **11**, fluorescent granules coincide with light-contrast vesicles that are clearly recognized in bright-field images (Fig. 2) and from our experience [17,18] correspond to lipid droplets. Colocalization of Nile Red, a fluorescent probe of lipid droplets, and CIBC (Fig. 3) confirms unambiguously the conclusion of the origin of the granular pattern for **1**–**10**. Compounds **1**–**10** do not accumulate in lysosomes (Fig. 3).

The distribution of the granular fluorescence of **11** does not coincide with the lipid droplets, as they are observed in the bright-field images of cells (Fig. 2). Compound **11** is supposed to accumulate in lysosomes but we are not able to confirm this conclusion with the colocalization analysis because an intracellular fluorescence signal of **11** is lower than the detection limit of the CSI installation and LSCM 510META.

Enhanced staining of a perinuclear region is related to CIBC accumulation in the Golgi apparatus as demonstrated with BODIPY ceramide (Fig. 3). Affinity to the Golgi apparatus decreases in the order **10** ≈ **5** > **1** > **2** ≈ **3** ≈ **4** ≈ **5** ≈ **6** > **8** ≈ **9** > **11**. For most of compounds, this type of localization is supplemented with distinct staining of nuclear membranes or some structures tightly associated with the nuclear membrane (Fig. 2). There is no selective accumulation of CIBCs in mitochondria, since the pattern of mitochondrion staining with Rh123 does not resemble distribution of CIBCs in cytoplasm (Fig. 3). Taking into account a high affinity of CIBCs to lipid structures, weak binding of CIBCs to different cellular membranes (including endoplasmic reticulum and mitochondrial and lysosomal membranes) cannot be excluded. Intracellular localization was the same whether CIBCs were added to cells from dimethyl sulfoxide or from CrEL solution (Fig. 3).

The studied compounds are characterized by significant differences in local intracellular concentrations of the monomeric photoactive form (see intensity scales in Fig. 2). Evidently, high cellular uptake of photosensitizer is of critical importance for its photodynamic activity along with other factors such as Φ_Δ and intracellular localization. Accordingly, dependencies of intracellular accumulation on extracellular concentration were measured for **5**, **6**, **8,** and **10** (Fig. 4). It is clearly seen that the average intracellular concentration of CIBC is very responsive to the extracellular concentrations of the compounds. An increase in extracellular concentration of CIBC to 1 μM is accompanied with a linear growth of its intracellular concentration. A moderate saturation of uptake is observed at higher concentrations of CIBC in the medium. Accordingly, a distribution ratio (DR), a slope of the linear section of uptake, was measured for the HeLa cells incubated with 1 μM CIBC for 3 h (Table 1). It should be noted that the monomeric photoactive form of photosensitizer contributes to DR, when it is estimated with the CSI technique. As shown above the aggregated dye is not active and does not fluoresce. All CIBCs (except for cationic **11**) surpass **1** in DR. The highest DR values were registered for the compounds with preferential accumulation in the Golgi apparatus (**5**) and with a

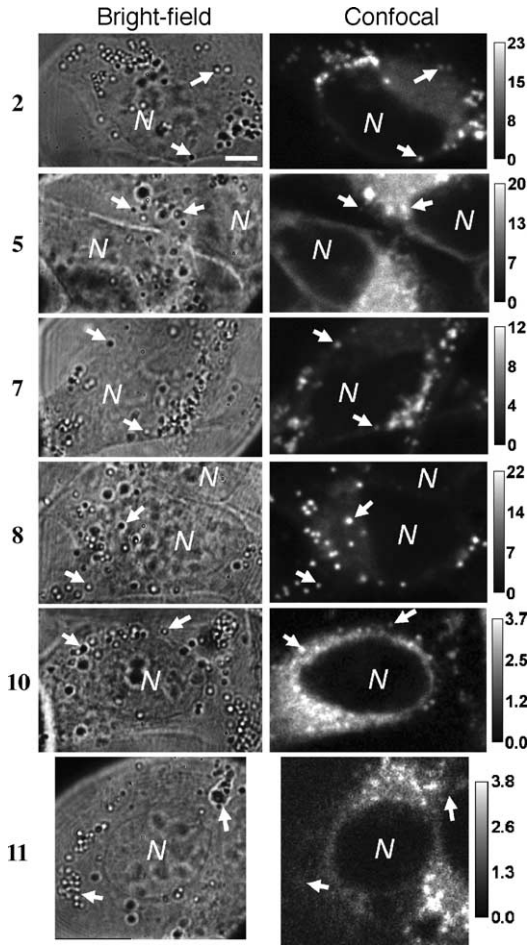

Fig. 2. Typical intracellular distributions of **2**, **5**, **7**, **8, 10,** and **11** in living HeLa cells as measured with NIR-LSCM. Localization patterns of **3**, **4** and **6** are very similar to that of **2**. Cells were exposed to 1 μM of each derivative for 3 h. N marks the nucleus; arrows indicate some of the lipid droplets; bar represents 5 μm. Intensity scales show the estimated concentration of photosensitizer in μM.

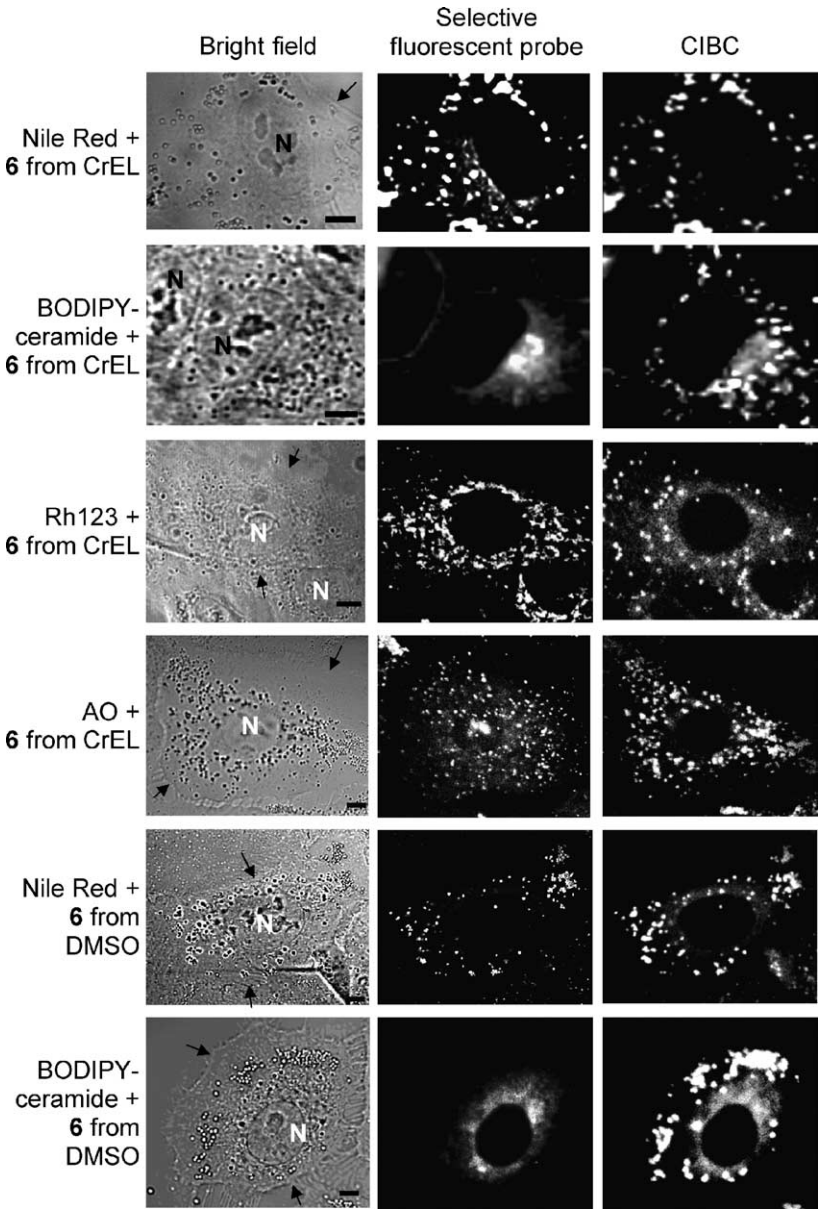

Fig. 3. Localization of CIBC in A549 cells. Cells were loaded with **6** from CrEL emulsion or from dimethyl sulfoxide and stained with Nile Red (stains lipid droplets) or BODIPY ceramide (stains Golgi apparatus) or Rh123 (stains mitochondria) or AO (stains lysosomes) as described under Materials and methods. Bright-field images of cells and confocal fluorescent images of selective fluorescent probes and **6** are presented. Note that (i) the spotted distribution of **6** coincides exactly with the localization of lipid droplets stained with Nile Red; (ii) the distribution of the brightest diffuse signal of **6** in the perinuclear region coincides well with the localization of the Golgi apparatus stained with BODIPY ceramide. Bar represents 5 μm; N marks nuclei; arrows indicate cell boundary.

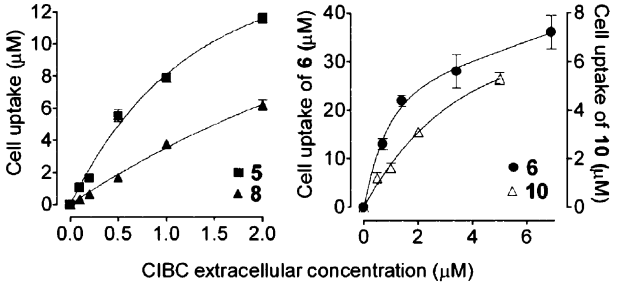

Fig. 4. Intracellular uptake of CIBCs depends linearly on extracellular concentration at extracellular concentrations below 1 μM and tends to saturate at higher concentrations. HeLa cells were incubated with **5**, **6**, **8,** or **10** for 3 h in complete medium. Cell uptake was determined as average cytoplasmic concentration of CIBC using NIR-LSCM.

mixed localization (**3**, **4**, **6**). Compounds **8** and **9** that accumulate selectively in lipid droplets have moderate DR (Table 1), but their local concentration within the lipid droplets is very high (Fig. 2). Low DR was observed for **7, 10,** and **11** because of an improper combinations of substituents.

Times for a 50% release of the dye from the cells were found to be rather similar for different CIBC: 37 ± 2, 46 ± 3, 59 ± 5, 52 ± 7, and 53 ± 8 min for **2**, **5**, **7**, **8,** and **10**, respectively. Thus, the considered substituents do not affect efflux kinetics. At the same time, the intracellular distribution of **2** and **5** but not **7**, **8,** and **10** changed during efflux. Compound **2** accumulates in the Golgi apparatus and lipid droplets (Table 1, Fig. 2), but it localizes predominantly in the

Golgi apparatus after 2 h efflux (data not shown) because its release from lipid droplets occurs faster than from the Golgi apparatus. Fast efflux from the Golgi apparatus and long–term retention in lipid droplets are a property of **5**.

State of cellular organelles after irradiation

A state of cellular organelles after the photodynamic treatment was examined for **2**, **5**, **6,** and **8,** and the resulting

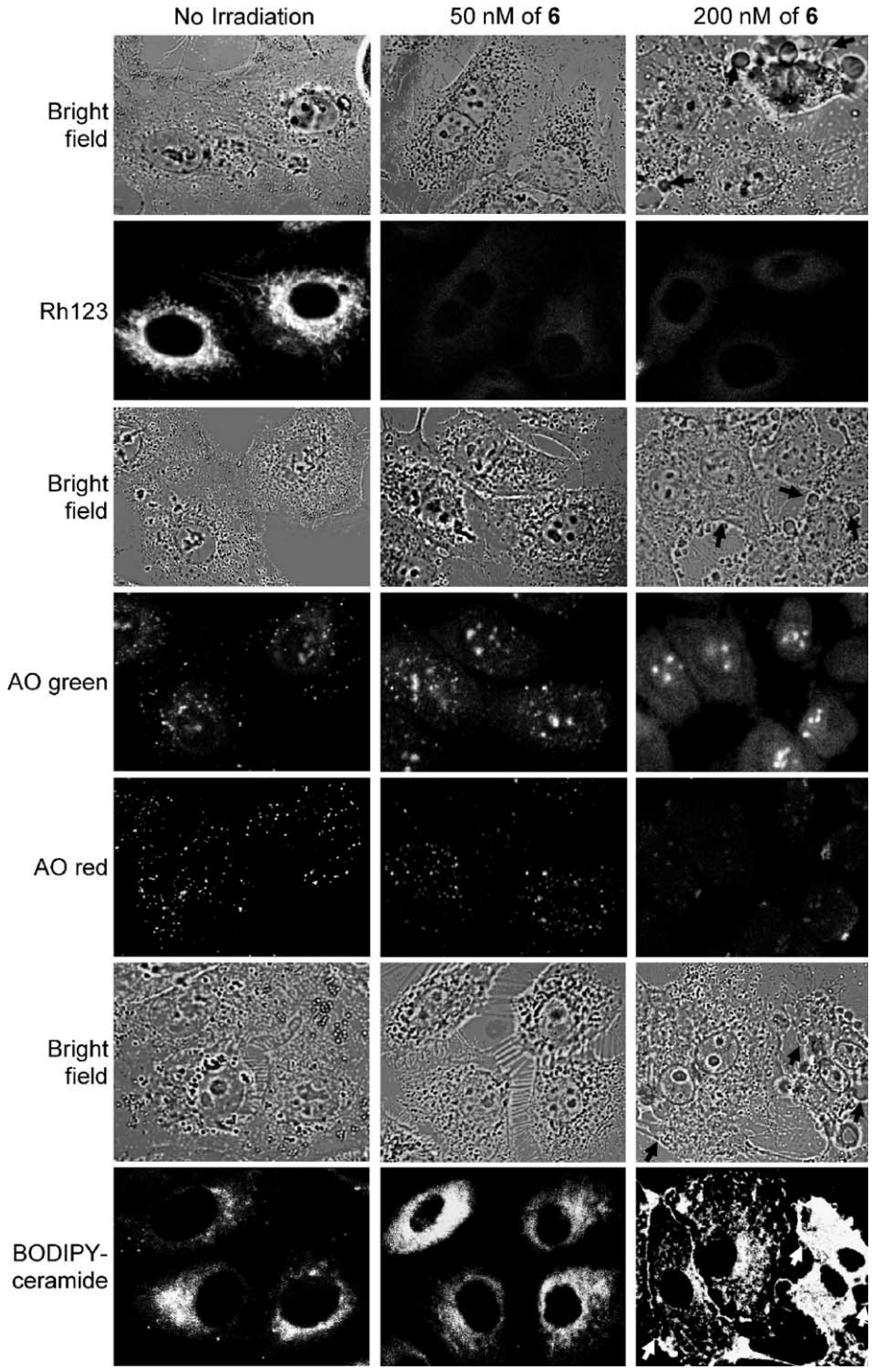

Fig. 5. Influence of subphototoxic (50 nM of **6**) and phototoxic (200 nM of **6**) regimes of photodynamic treatments on the state of mitochondria, lysosomes, and lipid transport in A549 cells. Cells were incubated with 50 nM (subphototoxic regime) or 200 nM (phototoxic regime) of **6** for 3 h, placed in the dye-free medium, and irradiated (11 ± 1 mW/cm^2, 15 min). One hour later, mitochondria, lysosomes, and Golgi apparatus of cells were stained with Rh123, AO, and BODIPY ceramide, respectively, as described in under Materials and methods and analyzed with LSCM 510META. Fluorescent images of irradiated and nonirradiated cells shown on the same line were recorded under identical conditions, and the relative signal intensities can be directly compared. Bright-field images of cells are situated above the corresponding fluorescent images. Arrows indicate cells subjected to lysis. AO red, distribution of the red fluorescence of aggregated AO (emission maximum 640 nm) in lysosomes. AO green, distribution of the green fluorescence of monomeric AO (emission maximum 530 nm).

patterns were found to be rather similar despite differences in the intracellular distribution of these CIBCs. The results of the study are illustrated here for **6** (Fig. 5).

When cells were irradiated under conditions that induced about 50% inhibition of cell growth 24 h after the irradiation ("subphototoxic" conditions), the intensity of mitochondrial staining with Rh123 reduced sharply, and the filamentous structure of mitochondria was not observed anymore (Fig. 5). Since mitochondrial staining with Rh123 depends on a mitochondrial potential [27], one can conclude that the mitochondrial potential decreases considerably in response to the subphototoxic treatment of cells loaded with CIBCs. It is known that an elevated level of ROS can induce the opening of nonspecific pores in the inner mitochondrial membrane and an activation of mitochondrial mechanisms leading to the decrease in the ROS concentration [28]. Mitochondrial potential is absent, when pores are open.

The subphototoxic regime did not affect lysosome staining with AO (Fig. 5). The lipid transport was not disturbed, and characteristic staining of the Golgi apparatus with BODIPY ceramide was still observed in the cells (Fig. 5).

When cells were irradiated under conditions that induced about 90% inhibition of cell growth 24 h after the irradiation ("phototoxic" conditions), the drop in the mitochondrial potential was accompanied with the disappearance of AO-stained lysosomes (Fig. 5). Punctated lysosome-associated fluorescence of AO vanished, including a red fluorescence of aggregated AO (emission maximum 640 nm) and a green fluorescence (emission maximum 530 nm) of monomeric AO. It was substituted with the diffuse cytoplasmic fluorescence of monomeric AO. This fact indicates a photoinduced permeabilization of lysosomal membrane and/or disruption of lysosomes. Transport of BODIPY ceramide from plasma membrane to the Golgi apparatus was noticeably disturbed with the phototoxic treatment: diffuse staining of cytoplasmic structures instead of accumulation in the Golgi apparatus was observed (Fig. 5). Lysis of many cells was observed 1 h after irradiation (Fig. 5). The dose of ROS produced during

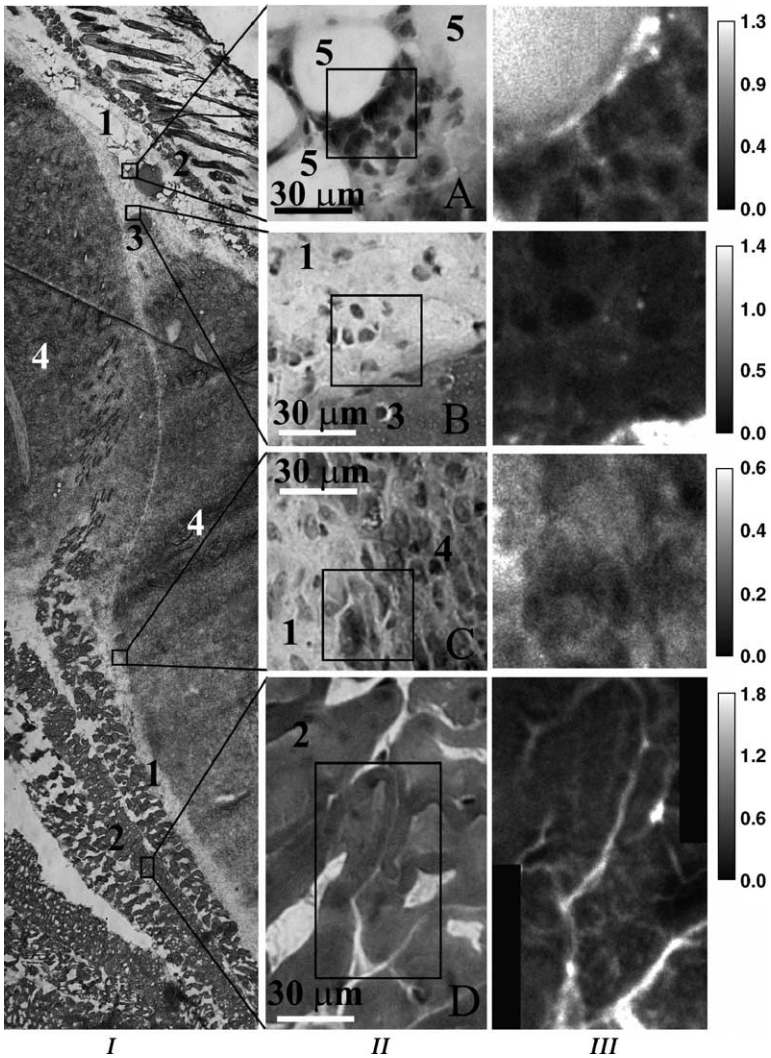

Fig. 6. Distribution of **8** in murine tissues at 3 h after injection as measured with NIR-LSCM. Columns I and II are the bright-field images of a hematoxylin-eosin-stained tissue slice at different magnifications. 1, connective tissue; 2, muscle fibers; 3, blood vessels, 4, tumor; and 5, fatty cells. Areas A–D in column II correspond to the regions marked in column I with rectangles. Column III is confocal fluorescence images of the distribution of **8** in the areas marked with rectangles in column II. Scales show estimated concentrations of **8** in μM.

Table 2
Distribution of CIBCs in tumor and surrounding tissues

Tissue structure	Compound			
	2	**5**	**7**	**8**
Tumor cells	44 ± 20[a]	100 ± 35	75 ± 45	290 ± 90
Connective tissue	115 ± 80	150 ± 75	40 ± 15	330 ± 80
Muscle fibers	110 ± 75	310 ± 195	80 ± 65	500 ± 300
Blood vessels	N/D[b]	450 ± 230	250 ± 95	1300 ± 600
Adipose tissue	295 ± 70	110 ± 50	80 ± 30	600 ± 300
Dermis	90 ± 60	170 ± 50	60 ± 20	900 ± 500
Hair follicle	N/D	290 ± 160	70 ± 55	1200 ± 700
Epidermis	60 ± 40	200 ± 130	45 ± 15	41 ± 28

[a] Estimated concentrations of photosensitizer in nM (mean ± SD).
[b] N/D, this tissue structure was not detected in the studied specimens.

phototoxic treatment was high enough to induce simultaneously an inactivation of mitochondria, a disturbance of lipid transport, a damage of lysosomes, and even lysis of plasma membrane.

Tissue distribution of CIBC

Detailed distributions of **2**, **5**, **7**, and **8** in murine malignant tissues were successfully pictured with NIR-LSCM. Typical tissue distributions of **8** are shown in Fig. 6. The concentration of **8** is highest in blood vessels. It is also high in the structures that are well supplied with blood (muscles, hair follicle). The concentration of **8** declines and approaches to a constant three-to fivefold reduced level within 20–50 μm from the blood vessels. Compound **8** accumulates considerably in dermis, fat cells, endomysium, and peritumoral connective tissue, penetrates efficiently in tumor, and stains it rather uniformly (Fig. 6, Table 2).

Tissue distribution patterns observed for **2**, **5,** and **7** are qualitatively similar to the tissue distribution of **8**, but **2**, **5,** and **7** have reduced concentrations in tissues and slightly different affinity to particular tissue structures (Table 2). Remarkably, compound **5** is not able to penetrate inside fat cells in contrast to **2**, **7,** and **8**. It accumulates at the surface of fat cells.

The concentration of **8** in the studied tissues is several-fold higher than that of **2**, **5,** and **7** (Table 2).

Discussion

Our study confirms that CIBCs surpass bacteriochlorins in photophysical properties: they are photostable, have intensive absorption in the NIR region, and possess efficient photoinduced singlet oxygen generation (Table 1). At the same time, many of the PDT-relevant properties depend on the substituent groups, and in vivo photosensitizing activity of CIBCs can be considerably improved, optimizing the structure of substituents.

It is worth noting that out of the PDT-useful region CIBCs have reduced absorption as compared to many other porphyrin-based photosensitizers. Integral absorption of CIBCs is distributed as follows: 35% in the 720–870 nm region (PDT-useful range) and 65% in the 350–720 nm range. For comparison, 20 and 80% of the integral absorption of chlorin p6 and pyropheophorbide derivatives are in the 600–700 (PDT-useful range) and 350–600 nm regions, respectively. Therefore, the risk of generalized posttherapy photosensitization induced by sunlight is reduced in the case of CIBCs.

The RNO/histidine assay demonstrates that the monomeric membrane-bound form of CIBC produces singlet oxygen, which can either release in the aqueous phase and oxidize there biological molecules or participate in the oxidation of lipids and membrane-bound molecules. Φ_Δ of CIBC are high (Table 1) and exceed Φ_Δ of **1** and bacteriochlorophyll *a* in liposomes (Φ_Δ = 0.33 [29]). Substituents conjugated at the fused imide ring via N–N bond (compounds **8**–**11**) reduce Φ_Δ, whereas other studied substituents do not affect Φ_Δ. Strikingly, Φ_Δ of **2**–**7** are of the same value as Φ_Δ of the best photosensitizers absorbing in the 650–700 nm region [30,31].

Data of our investigation show that intracellular localization of CIBC can be controlled with appropriate substituents. Parent compound **1** has roughly equal affinity to the Golgi apparatus and lipid droplets (Table 1). Lipid droplets, also known as lipid bodies or lipid particles, consist of a highly hydrophobic core of neutral lipids, mainly triacylglycerols or steryl esters (or both), which is enveloped by a phospholipid monolayer with only a small amount of proteins embedded [32]. Accordingly, when a balance between polar and hydrophobic substituents shifts to the latter, CIBC accumulate preferably in the lipid droplets. More amphiphilic or polar compounds like **5** and **10** are selectively transported into the Golgi apparatus. Cationic **11** is most probably targeted to lysosomes. Sometimes intracellular sorting of CIBC is not so evident. For example, the R_2 amino group of **9** looks more favorable for accumulation in the Golgi apparatus, but **9** is found in the lipid droplets (Table 1).

With respect to intracellular localization we observe a direct similarity between CIBCs and CICs studied us earlier [16–18]. Negatively charged CICs and those bearing polar substituents accumulated in the Golgi apparatus, whereas neutral hydrophobic CICs were selectively targeted to lipid droplets. Similarity in intracellular localization is very reasonable here, since the chromophore structure of CIBC and CIC is not very different.

Surprisingly, the neutral hydrophobic alkyl ether derivative **12** was reported to localize in lysosomes, whereas neutral hydrophobic compounds **13**–**15** (Fig. 1) were found in mitochondria [11]. It should be noted that the conclusions concerning the intracellular localization of **12**–**15** look dubious in part. First, lysosomal localization was probed with fluorescein-labeled latex beads, while fluorescein fluorescence is known to be quenched at acidic pH, and this fluorophore is hardly suitable for lysosome tracing. Second, intracellular localization was examined with conventional fluorescence microscopy, while LSCM was required to resolve overlapping signals coming from different cellular layers. If, nevertheless, these conclusions are true, a set of different CIBC derivatives could be recommended as a useful tool for investigating features of photosensitizing reactions and cellular processes initiated selectively in different cellular compartments: lysosomes, Golgi apparatus, lipid droplets, and mitochondria.

Efflux rates were found to be similar for **2**, **5**, **7**, **8,** and **10,** but structure-related features were revealed in the intracellular

distribution of CIBCs during efflux. Release occurred much faster from lipid droplets than from the Golgi apparatus for **2** and vice versa for **5**, whereas the intracellular distribution of **7**, **8,** and **10** did not change during efflux. Here tight bindings of **2** in the Golgi apparatus and **5** in lipid droplets are in contrast with their predominant localization during uptake.

DR is another important parameter that is affected by substituents (Table 1). Substitution of 3-acetyl group with aliphatic ethers increased considerably intracellular accumulation of **4**, **5,** and, especially, **3** and **6**. The studied substituents at the fused imide ring (compounds **8**–**11**) were less efficient in promoting uptake. The substituents in **10** and **11** were the least suitable for intracellular penetration and/or accumulation of CIBC.

It is expected that higher intracellular concentrations of photosensitizer must provide higher photoinduced toxicity. This rule is working for each of **1**–**10** separately: an increase in extracellular concentration is accompanied with an increase in phototoxicity, and intracellular concentration of CIBC is directly proportional to its extracellular concentration. At the same time, very different intracellular concentrations of **2**–**7** provide the same phototoxicity as follows from comparison of DR and IC_{90} values (Table 1). These compounds have similar absorption characteristics, equal Φ_Δ, and even intracellular localizations of **2**–**4**, **6,** and **7** are very similar. Therefore, there are additional factors that modulate overall photosensitizing effect. One may suppose that critical molecular targets and/or singlet oxygen quenchers have microheterogeneous distribution within particular cellular compartments/organelles, and there is hardly any predictable influence of substituents on the ability of the photosensitizer to accumulate in immediate proximity to these targets and quenchers. For example, if unsaturated lipid bonds are the critical targets, then efficiency of their photoinduced oxidation depends at least on the mode of membrane binding (surface binding, deep intercalation into bilayer, etc.), which is realized for the photosensitizer.

Compounds **1** and **9**–**11** have reduced photosensitizing activity, and this fact is in strict accordance with the characteristics of **1** and **9**–**11** listed in Table 1. Decreased absorption (compounds **1**, **9**) and small Φ_Δ (**1**, **9, 10,** and, especially, **11**) and reduced DR (**1**, **10** and **11**) result in the low photoinduced cytotoxicity.

Using data of Table 1, lethal doses of CIBC-generated singlet oxygen were evaluated. Here a lethal dose $LD_{90}(^1O_2)$ means the amount of singlet oxygen per volume unit of cell generated during irradiation that provides 90% cytotoxicity. The $LD_{90}(^1O_2)$) value can be estimated as

$$LD_{90}(^1O_2) \approx \Phi_\Delta \cdot C_{PS} \cdot \left(\int \sigma(\lambda) d\lambda / \Delta\lambda \right) \cdot N_{h\nu}, \quad (2)$$

where C_{PS} is intracellular concentration of photosensitizer that corresponds to IC_{90}, $\int\sigma(\lambda)d\lambda$ is absorption cross section integrated over the irradiation spectral window (700–1000 nm), $\Delta\lambda$ is a width of this window, and $N_{h\nu}$ is the number of photons per area unit passed during irradiation time. C_{PS} is calculated as IC_{90} multiplied by DR. Absorption cross section (in cm^2) can be derived from molar extinction coefficient as $\sigma = 3.82 \times 10^{-21} \times \varepsilon$. $N_{h\nu}$ can be calculated as quotient of light energy density (10 J/cm^2) and average energy of a photon (λ = 900 nm, $h\nu = 2.32 \times 10^{-19}$ J). Finally,

$$LD_{90}(^1O_2) \approx 4.9 \times 10^{-4} \cdot \Phi_\Delta \cdot IC_{90} \cdot DR \cdot \int \varepsilon(\lambda) d\lambda. \quad (3)$$

The $LD_{90}(^1O_2)$ values for the studied compounds are presented in Table 1. Average $LD_{90}(^1O_2)$ is 0.22 mM. This value is very close to the lethal dose of singlet oxygen estimated for Photofrin in tumor spheroids (0.32 mM [33]), whereas 1 mM was reported for etiopurpurin I [34], and 12 mM was an alternative value for Photofrin [35].

In fact, the $LD_{90}(^1O_2)$ value characterizes the damaging efficiency of singlet oxygen produced by the photosensitizer and seems to depend on the microenvironment, namely proximity to critical molecular targets and quenchers. Direct comparison of the lethal doses of singlet oxygen estimated by various researchers is not valid because of different approaches and experimental conditions used, but it can be done for **1**–**10**. Thus, the damaging efficiency of singlet oxygen produced by **7** is highest and surpasses the same parameter of other CIBCs by two to seven times (Table 1).

Submicrometer tissue distribution of photosensitizers, which absorb and fluoresce at wavelengths longer than 750 nm, is reported for the first time. It became possible due to application of a highly sensitive NIR-LSCM developed by us. This investigation revealed that CIBCs accumulate in both tumor cells and surrounding tissues (Fig. 6, Table 2). Such a distribution predefines the combined action of two mechanisms of PDT: direct tumor cell damage and destruction of tumor trophic-supporting tissues. High concentrations of **5**, **7,** and **8** in blood vessels indicate that the vascular occlusion could be also observed after PDT was performed within 3 h after intravenous injection of CIBCs. In vivo PDT experiments with CIBCs are in progress now, and they are supported with extensive fluorescence microscopy analysis, which is aimed at optimization of a PDT protocol and revealing interrelations between features of tissue distribution and photosensitizing efficacy of different CIBCs.

In conclusion, photodynamic properties of CIBCs are promising for antitumor PDT. Our findings highlight the importance of CIBC structure optimization as a way of targeting photosensitizers to specific cellular organelles and improving its cellular and tumor accumulation. Cellular and tissue fluorescence microscopy realized with NIR-LSCM is a powerful tool for screening and rational development of NIR photosensitizers.

Acknowledgments

This work was supported by Grants INTAS-01-0461, RFBR-02-04-22001, and RFBR-04-04-48372. G.V.S. was supported by a FEBS Summer Fellowship.

References

[1] Dougherty, T. J.; Gomer, C. J.; Henderson, B. W.; Jori, G.; Kessel, D.; Korbelik, M.; Moan, J.; Peng, Q. Photodynamic therapy. *J. Natl. Cancer Inst.* **90:**889–905; 1998.

[2] Hasan, T.; Ortel, B.; Moor, A. C. E.; Pogue, B. W. Photodynamic therapy of cancer. In: Kuffe, D. W.; Pollock, R. E.; Weichselbaum, R. R.; Bast, R. C., Jr.; Gansler, T. S.; Holland, J. F.; Frei, E., III, eds. *Cancer medicine*. American Cancer Society and BC Decker Inc.; 2003: 605-622.

[3] Oertel, M.; Schastak, S. I.; Tannapfel, A.; Hermann, R.; Sack, U.; Mossner, J.; Berr, F. Novel bacteriochlorin for high tissue-penetration: photodynamic properties in human biliary tract cancer cells in vitro and in a mouse tumour model. *J. Photochem. Photobiol. B.* **71:**1–10; 2003.

[4] Kelleher, D. K.; Thews, O.; Scherz, A.; Salomon, Y.; Vaupel, P. Perfusion, oxygenation status and growth of experimental tumors upon photodynamic therapy with Pd-bacteriopheophorbide. *Int. J. Oncol.* **24:**1505–1511; 2004.

[5] Mazor, O.; Brandis, A.; Plaks, V.; Neumark, E.; Rosenbach-Belkin, V.; Salomon, Y.; Scherz, A. WST11, a novel water-soluble bacteriochlorophyll derivative; cellular uptake, pharmacokinetics, biodistribution, and vascular targeted photodynamic activity against melanoma tumors. *Photochem. Photobiol.* **81:**342–351; 2005.

[6] Rovers, J. P.; de Jode, M. L.; Rezzoug, H.; Grahn, M. F. In vivo photodynamic characteristics of the near-infrared photosensitizer 5,10,15,20-tetrakis(m-hydroxyphenyl) bacteriochlorin. *Photochem. Photobiol.* **72:**358–364; 2000.

[7] Li, G.; Grahm, A.; Chen, Y.; Dobhal, M. P.; Morgan, J.; Zheng, G.; Kozyrev, A.; Oseroff, A.; Dougherty, T. J.; Pandey, R. K. Synthesis, comparative photosensitizing efficacy, human serum albumin (site II) binding ability, and intracellular localization characteristics of novel benzobacteriochlorins derived from vic-dihidroxybacteriochlorins. *J. Med. Chem.* **46:**5349–5359; 2003.

[8] Mironov, A. F.; Grin, M. A.; Tsiprovskiy, A. G.; Kachala, V. V.; Karmakova, T. A.; Plyutinskaya, A. D.; Yakubovskaya, R. I. New bacteriochlorin derivatives with a fused N-aminoimide ring. *J. Porphyr. Phthalocya.* **7:**725–730; 2003.

[9] Mironov, A. F.; Grin, M. A.; Tsyprovskiy, A. G. Synthesis of the first N-hydroxycycloimide in the bacteriochlorophyll a series. *J. Porphyr. Phthalocya.* **6:**358–361; 2002.

[10] Mironov, A. F.; Kozyrev, A. N.; Brandis, A. S. Sensitizers of second generation for photodynamic therapy of cancer based on chlorophyll and bacteriochlorophyll derivatives. *Proc. SPIE* **1922:**204–208; 1992.

[11] Chen, Y.; Grahm, A.; Potter, W.; Morgan, J.; Vaughan, L.; Bellnier, D. A.; Henderson, B. W.; Oseroff, A.; Dougherty, T. J.; Pandey, R. K. Bacteriopurpurinimides: highly stable and potent photosensitisers for photodynamic therapy. *J. Med. Chem.* **45:**255–258; 2002.

[12] Chen, Y.; Sumlin, A.; Morgan, J.; Gryshuk, A.; Oseroff, A.; Henderson, B. W.; Dougherty, T. J.; Pandey, R. K. Synthesis and photosensitizing efficacy of isomerically pure bacteriopurpurinimides. *J. Med. Chem.* **47:**4814–4817; 2004.

[13] Mironov, A. F.; Grin, M. A.; Tsiprovskii, A. G.; Segenevich, A. V.; Dzardanov, D. V.; Golovin, K. V.; Tsygnkov, A. A.; Shim, Y. K. New photosensitizers of bacteriochlorin series for photodynamic cancer therapy. *Russ. J. Bioorg. Chem.* **29:**214–221; 2003.

[14] Mironov, A. F.; Grin, M. A.; Tsiprovskii, A. G.; Titeev, R. A.; Nizhnik, E. A.; Lonin, I. S. Synthesis of cationic bacteriochlorins. *Mendeleev Commun.* **5:**204–207; 2004.

[15] Sharonov, G. V.; Karmakova, T. A.; Kassies, R.; Plutinskaja, A. D.; Grin, M. A.; Yakubovskaja, R. I.; Mironov, A. F.; Refregiers, M.; Maurizot, J.-C.; Vigny, P.; Otto, C.; Feofanov, A. V. Cellular-and tissue distribution of near infrared photosensitizers based on cycloimide derivatives of bacteriochlorin (abstract). *Chem. Listy* **98:**s17; 2004.

[16] Feofanov, A.; Grichine, A.; Karmakova, T.; Pljutinskaja, A.; Lebedeva, V.; Filyasova, A.; Yakubovskaya, R.; Mironov, A.; Egret-Charlier, M.; Vigny, P. Near-infrared photosensitizer on the basis of cycloimide derivative of chlorin p6: 13,15-N-(3′-hydroxypropyl)cycloimide chlorin p6. *Photochem. Photobiol.* **75:**633–643; 2002.

[17] Feofanov, A.; Sharonov, G.; Grichine, A.; Karmakova, T.; Pljutinskaja, A.; Lebedeva, V.; Ruziyev, R.; Yakubovskaya, R.; Mironov, A.; Refregiers, M.; Maurizot, J.-C.; Vigny, P. Comparative study of photodynamic properties of 13,15-N-cycloimide derivatives of chlorin p6. *Photochem. Photobiol.* **79:**172–188; 2004.

[18] Feofanov, A. V.; Nazarova, A. I.; Karmakova, T. A.; Pljutinskaja, A. D.; Grichine, A. I.; Yakubovskaya, R. I.; Lebedeva, V. S.; Ruziev, R. D.; Mironov, A. F.; Maurizot, J.-C.; Vigny, P. Photobiological properties of 13,15-*N*-(carboxymethyl)-and 13,15-*N*-(2-carboxyethyl)cycloimide derivatives of chlorin p6. *Russ. J. Bioorg. Chem.* **30:**374–384; 2004.

[19] Karmakova, T.; Feofanov, A.; Nazarova, A.; Grichine, A.; Yakubovskaya, R.; Luk'yanets, E.; Maurizot, J.-C.; Vigny, P. Distribution of metal-free sulfonated phthalocyanine in subcutaneously transplanted murine tumors. *J. Photochem. Photobiol. B* **75:**81–87; 2004.

[20] Feofanov, A. V.; Karmakova, T. A.; Grishine, A. I.; Fomina, G. I.; Nazimov, I. V.; Yakubovskaya, R. I.; Egret-Charlier, M.; Vigny, P. Distribution and interactions of photosens in murine Ehrlich adenocarcinoma—Fluorescent spectral imaging approach. In: Kotyk, A., ed. *Fluorescence Microscopy and Fluorescent Probes*, volume 3. Espero Publishing, Usti nad Labem, pp. 323–330; 1999.

[21] Blum, A.; Grossweiner, L. I. Singlet oxygen generation by hematoporphyrin IX, uroporphyrin I and hematoporphyrin derivative at 546 nm in phosphate buffer and in the presence of egg phosphatidylcholine liposomes. *Photochem. Photobiol.* **41:**27–32; 1985.

[22] Bors, W.; Saran, M.; Lengfelder, E.; Michel, C.; Fuchs, C.; Frenzel, C. Detection of oxygen radicals in biological reactions. *Photochem. Photobiol.* **28:**629–638; 1978.

[23] Gandin, E.; Lion, Y.; Van de Vorst, A. Quantum yield of singlet oxygen production by xanthene derivatives. *Photochem. Photobiol.* **37:**271–278; 1983.

[24] Carmichael, J.; DeGraff, W. G.; Gazdar, A. F.; Minna, J. D.; Mitchell, J. B. Evaluation of a tetrazolium-based semiautomated colorimetric assay: assessment of chemosensitivity testing. *Cancer Res.* **47:**936–942; 1987.

[25] Feofanov, A.; Charonov, S.; Fleury, F.; Kudelina, I.; Nabiev, I. Localization and molecular interactions of mitoxantrone within living K562 cells as probed by confocal spectral imaging analysis. *Biophys. J.* **73:**3317–3327; 1997.

[26] Feofanov, A.; Charonov, S.; Fleury, F.; Kudelina, I.; Nabiev, I. Quantitative confocal spectral imaging analysis of mitoxantrone within living K562 cells: intracellular accumulation and distribution of monomers, aggregates, naphtoquinoxaline metabolite and drug-target complexes. *Biophys. J.* **73:**3328–3336; 1997.

[27] Chen, L. B. Fluorescent labeling of mitochondria. In: Wang, Y.-L.; Lansing, T. D., eds. *Fluorescent Microscopy of Living Cells in Culture. Part A*. Academic Press, San Diego, pp. 103–123; 1989.

[28] Skulachev, V. P. Uncoupling: new approaches to an old problem of bioenergetics. *Biochim. Biophys. Acta* **1363:**100–124; 1998.

[29] Hoebeke, M.; Damoiseau, X. Determination of the singlet oxygen quantum yield of bacteriochlorin a: a comparative study in phosphate buffer and aqueous dispersion of dimiristoyl-L–phosphatidylcholine liposomes. *Photochem. Photobiol. Sci.* **1:**283–287; 2002.

[30] Nyman, E. S.; Hynninen, P. H. Research advances in the use of tetrapyrrolic photosensitizers for photodynamic therapy. *J. Photochem. Photobiol. B* **73:**1–28; 2004.

[31] Spiller, W.; Kliesch, H.; Wohrle, D.; Hackbarth, S.; Roder, B.; Schnurpfeil, G. Singlet oxygen quantum yields of different photosensitizers in polar solvents and micellar solutions. *J. Porphyr. Phtalocya.* **2:**145–148; 1998.

[32] Zweytick, D.; Athenstaedt, K.; Daum, G. Intracellular lipid particles of eukaryotic cells. *Biochim. Biophys. Acta* **1469:**101–120; 2000.

[33] Nichols, M. G.; Foster, T. H. Oxygen diffusion and reaction-kinetics in the photodynamic therapy of multicell tumor spheroids. *Phys. Med. Biol.* **39:**2161–2181; 1994.

[34] Pogue, B. W.; Ortel, B.; Chen, N.; Redmond, R. W.; Hasan, T. A photobiological and photophysical-based study of phototoxicity of two chlorins. *Cancer Res.* **61:**717–724; 2001.

[35] Georgakoudi, I.; Nichols, M. G.; Foster, T. H. The mechanism of Photofrin photobleaching and its consequences for photodynamic dosimetry. *Photochem. Photobiol.* **65:**135–144; 1997.